

# A statistical study of gamma-ray burst afterglows measured by the *Swift* Ultra-violet Optical Telescope

S. R. Oates<sup>1</sup>, M. J. Page<sup>1</sup>, P. Schady<sup>1</sup>, M. de Pasquale<sup>1</sup>, T. S. Koch<sup>2</sup>, A. A. Breeveld<sup>1</sup>, P. J. Brown<sup>2</sup>, M. M. Chester<sup>2</sup>, S. T. Holland<sup>3,4,5</sup>, E. A. Hoversten<sup>2</sup>, N. P. M. Kuin<sup>1</sup>, F. E. Marshall<sup>3</sup>, P. W. A. Roming<sup>2</sup>, M. Still<sup>1</sup>, D. E. Vanden Berk<sup>2</sup>, S. Zane<sup>1</sup> and J. A. Nousek<sup>2</sup>

<sup>1</sup> Mullard Space Science Laboratory, University College London, Holmbury St. Mary, Dorking Surrey, RH5 6NT, UK; sro@mssl.ucl.ac.uk

<sup>2</sup> Department of Astronomy and Astrophysics, Pennsylvania State University, 104 Davey Laboratory, University Park, PA 16802

<sup>3</sup> Astrophysics Science Division, Code 660.1, NASA Goddard Space Flight Centre, 8800 Greenbelt Road, Greenbelt, Maryland 20771, USA

<sup>4</sup> Universities Space Research Association, 10211 Wincopin Circle, Suite 500, Columbia, Maryland 21044, USA

<sup>5</sup> Centre for Research and Exploration in Space Science and Technology, Code 668.8, NASA Goddard Space Flight Centre, 8800 Greenbelt Road, Greenbelt, Maryland 20771, USA

23 August 2021

## ABSTRACT

We present the first statistical analysis of 27 Ultra-violet Optical Telescope (UVOT) optical/ultra-violet lightcurves of Gamma-Ray Burst (GRB) afterglows. We have found, through analysis of the lightcurves in the observer’s frame, that a significant fraction rise in the first 500s after the GRB trigger, that all lightcurves decay after 500s, typically as a power-law with a relatively narrow distribution of decay indices, and that the brightest optical afterglows tend to decay the quickest. We find that the rise could either be produced physically by the start of the forward shock, when the jet begins to plough into the external medium, or geometrically where an off-axis observer sees a rising lightcurve as an increasing amount of emission enters the observers line of sight, which occurs as the jet slows. We find that at 99.8% confidence, there is a correlation, in the observed frame, between the apparent magnitude of the lightcurves at 400s and the rate of decay after 500s. However, in the rest frame a Spearman Rank test shows only a weak correlation of low statistical significance between luminosity and decay rate. A correlation should be expected if the afterglows were produced by off-axis jets, suggesting that the jet is viewed from within the half-opening angle  $\theta$  or within a core of uniform energy density  $\theta_c$ . We also produced logarithmic luminosity distributions for three rest frame epochs. We find no evidence for bimodality in any of the distributions. Finally, we compare our sample of UVOT lightcurves with the X-ray Telescope (XRT) lightcurve canonical model. The range in decay indices seen in UVOT lightcurves at any epoch is most similar to the range in decay of the shallow decay segment of the XRT canonical model. However, in the XRT canonical model there is no indication of the rising behaviour observed in the UVOT lightcurves.

**Key words:** gamma-rays: bursts

## 1 INTRODUCTION

Gamma-ray bursts (GRBs) release between  $10^{52}$  and  $10^{54}$  ergs during the prompt emission, which lasts from a few milliseconds to a few thousand seconds, and is followed by an afterglow, which is observed in the X-ray to radio range from as little as a few tens of seconds up to several months after the GRB trigger.

The energy is transported in a relativistic outflow (Meszaros & Rees 1997) that is likely anisotropic (Sari et al.

1999) and the energy is expected to be released by internal and external shocks. Internal shocks (Rees & Meszaros 1994) are thought to produce the prompt gamma-ray emission, while external shocks (Rees & Meszaros 1992) are thought to produce the afterglow. Internal shocks occur when shells of material, which are thrown violently from the progenitor at different Lorentz factors, overtake each other. The external shocks are produced when the shells of material are decelerated by the external medium.

The short duration of the gamma-ray emission and

the rapid decay of the afterglow motivated the construction and launch of *Swift*, a rapid response satellite. *Swift* houses 3 instruments: the Burst Alert Telescope (BAT; Barthelmy et al. (2005)), the X-ray Telescope (XRT; Burrows et al. (2005)) and the Ultra-violet Optical Telescope (UVOT; Roming et al. (2005)). The energy ranges of the BAT and the XRT instruments are 15 keV - 350 keV and 0.2 - 10 keV, respectively, and the wavelength range of the UVOT is 1600Å-8000Å. The large field of view of the BAT (2 str), enables 1/6<sup>th</sup> of the sky to be searched for GRBs at any one time. Once a GRB has been detected by the BAT, *Swift* rapidly slews allowing the XRT and UVOT to observe the afterglow within a few tens of seconds after the BAT trigger.

Since launch, *Swift* has produced a large sample of UV/optical and X-ray lightcurves which begin soon after the trigger. The high detection rate with the XRT (96%; Burrows et al. 2008) allowed a large number of XRT lightcurves to be obtained within the first year. The systematic reduction of this sample resulted in the discovery of a 4 segment canonical XRT lightcurve (Zhang et al. 2006; Nousek et al. 2006). After 2 years of operation the UVOT, with a much lower detection rate than the XRT (26%; Roming et al. 2008), has detected more than 50 optical afterglows. This allows for the first time a systematic reduction and analysis of a significant sample of GRBs with optical afterglows observed with the UVOT and allows an investigation of their generic characteristics.

In this paper we present and analyze a sample of 27 UVOT lightcurves of GRB afterglows. In Section 2 we explain how we selected the sample of UVOT lightcurves and in Section 3 we describe how we systematically reduced and analyzed them. In Section 4 we present the results and in Section 5 we discuss our findings. Throughout the paper we will use the following flux convention,  $F \propto t^\alpha \nu^{\beta+1}$  with  $\alpha$  and  $\beta$  being the temporal and photon indices respectively. We assume the Hubble parameter  $H_0 = 70 \text{ km s}^{-1} \text{ Mpc}^{-1}$  and density parameters  $\Omega_\Lambda = 0.7$  and  $\Omega_m = 0.3$ . Unless stated otherwise, all uncertainties are quoted at  $1\sigma$ .

## 2 THE SAMPLE

To investigate the nature of GRB optical/UV lightcurves a large number of well sampled, good quality UVOT lightcurves were required. The sample was selected according to the following specific criteria: the optical/UV lightcurves must be observed in the v filter of the UVOT with a magnitude of  $\leq 17.8$ , UVOT observations must have commenced within the first 400s after the BAT trigger and the afterglow must have been observed until at least  $10^5$ s after the trigger. These selection criteria ensure the lightcurves have adequate signal to noise and cover both early and late time evolution. In addition to the above criteria, the colour of the afterglows must not evolve significantly with time, meaning that at no stage should the lightcurve from a single filter significantly deviate from any of the other filter lightcurves when normalized to the v filter. This ensures that a single lightcurve can be constructed from the UVOT multi-filter observations. Three GRBs, GRB 060218, GRB 060614

and GRB 060729 were excluded as they showed significant colour evolution.

In total 27 GRBs, which occurred between 1st January 2005 and 1st August 2007, fit the selection criteria. As there were no short GRBs that met the selection criteria, all the GRBs in this sample are long. Observations, for the majority of GRBs in this sample, began within the first 100s and the optical afterglow was detected until at least  $10^5$ s. Formally, GRB 050820a meets our selection criteria, but we have excluded this burst from the sample because the BAT triggered on a precursor of this GRB, and the main GRB took place as *Swift* entered the South Atlantic Anomaly (SAA) with the consequence that UVOT completely missed the early phase of the afterglow.

## 3 DATA REDUCTION

After the BAT has triggered on a GRB and *Swift* has slewed, the UVOT performs a sequence of pre-programmed exposures of varying length in multiple observing modes and filters designed to balance good time resolution and spectral coverage. Observations are performed in either event mode, where the arrival time and position are recorded for every photon detected, or in image mode, in which the data are recorded as an image accumulated over a fixed period of time. The pre-programmed observations begin with the settling and finding chart exposures. The settling exposure is not included in this analysis because the cathode voltage may still increase during the first few seconds. Two finding charts follow immediately after the settling exposure and these are observed in event mode with the v and white filters (as of the 7th November 2008 the finding charts are observed in u and white). The rest of the pre-programmed observations are a combination of event and image mode observations until  $\sim 2700$ s after the trigger, after which, only image mode is used. These observations are taken as a series of short, followed by medium and then long exposures, which are usually observed with all seven filters of the UVOT (white, v, b, u, uvw1, uvm2, uvw2). However, for some targets, the pre-programmed observation sequence may change or not be executed fully because of an observing constraint.

For GRB observations, the earliest part of the lightcurve is expected to show variability over the shortest timescales. As the finding charts, which are exposures of 100-400s, contain the earliest observations of the GRB, it is essential to obtain lightcurves from these event lists as well as obtaining lightcurves from the images.

### 3.1 Event and Image Data Reduction

To obtain the best possible lightcurves, we refined the astrometry of the event files before the count rates were obtained. The astrometry of the event list was refined by extracting an image every 10s and cross-correlating the stars in the image with those found in the USNO-B1 catalogue. The differences in RA and DEC between the stars in the image and the catalogue were converted into pixels and then applied to the position of every event in the event list during that particular 10s interval. This process was repeated until the end of each event list.

The images used in this paper were reprocessed by the

the Swift Science Data Center (SDC) for the UVOT GRB catalogue (Roming et al. 2008). These images were used because not all the image files in the Swift archive have been corrected for modulo-8 fixed pattern noise<sup>1</sup>; only those processed with *Swift* processing script version 3.9.9 and later have had this correction applied. For a small number of images, the aspect correction failed during the SDC processing and in these cases, the images were corrected using in-house aspect correction software.

An aperture of 5'', selected in order to be compatible with the UVOT calibration (Poole et al. 2008), was used to obtain the source count rates. However, for sources with a low count rate, it is more precise to use a smaller aperture (Poole et al. 2008). Therefore, below a threshold of 0.5 counts per second the source count rates were determined from 3'' radius apertures and the count rates were corrected to 5'' using a table of aperture correction factors contained within the calibration. The background counts were obtained from circular regions with radii, typically, of 20''. These regions were positioned, in each GRB field, over a blank area of sky. For each GRB, the same source and background regions were used to determine the count rates from the event lists and the images. The software used can be found in the software release, HEADAS 6.3.2 and the version 20071106 of the UVOT calibration files.

For each GRB, to maximise the signal to noise of the observed optical afterglow, the lightcurves from each filter in which the burst was detected were combined into one overall lightcurve. The lightcurves corresponding to the different filters were normalized to that in the *v* filter. This was possible because there was no significant colour evolution between the filters, which was one of the selection criteria described in Section 2. The normalization was determined by fitting a power-law to each of the lightcurves in a given time range simultaneously. The power-law indices were constrained to be the same for all the filters and the normalizations were allowed to vary between the filters. The ratios of the power-law normalizations were then used to normalize the count rates in each filter. The time range used to normalize the lightcurves was selected on the basis that the time range included data from all filters in which the burst was detected and (as far as possible) the lightcurves were in a power-law decay phase. Once the lightcurves were normalized, they were binned by taking the weighted average of the normalized count rates in time bins of  $\delta T/T = 0.2$ . The overall lightcurves were converted from *v* count rate to *v* magnitude using the zero point 17.89 (Poole et al. 2008). For many GRBs, the trigger time does not represent the true start of the gamma-ray emission. Therefore, the start of the gamma-ray emission was chosen as the start time of the T90 parameter. This parameter corresponds to the time in which 90% of the counts in the 15 keV - 350 keV band arrive at the detector (Sakamoto et al. 2008) and is determined from the gamma-ray event data for each GRB, by the BAT processing script. The results of the processing are publicly available and are provided for each trigger at [http://gcn.gsfc.nasa.gov/swift\\_gnd\\_ana.html](http://gcn.gsfc.nasa.gov/swift_gnd_ana.html). The difference between the trigger time and the start time of the T90 parameter is typically less than a few seconds. However, in

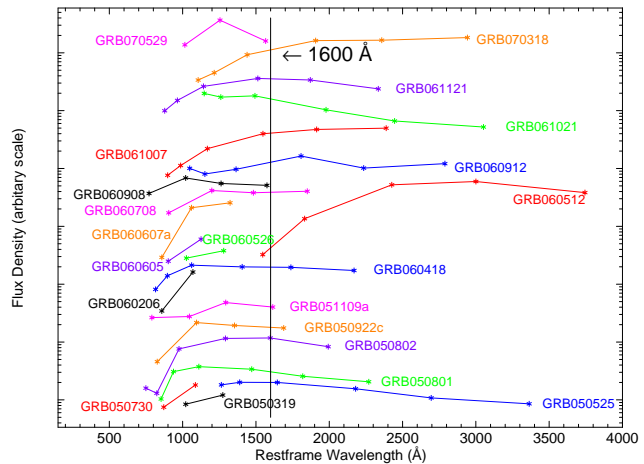


**Figure 1.** The rest frame relative flux SEDs for the 21 GRBs for which a luminosity lightcurve was produced. The relative flux for each filter of each GRB was determined by multiplying the relative count rate from Table 1 by the flux conversion factor given in Poole et al. (2008). The relative flux values have been corrected for Galactic extinction. The vertical line at 1600Å marks the rest frame wavelength at which the luminosity lightcurves were produced.

a minority of cases the difference is much larger, with the largest difference being 133.1s for GRB 050730.

### 3.2 Photometric Redshifts

Spectroscopic redshifts were obtained from the literature for 19 of the GRBs in the sample (see Table 1). For a further 4 GRBs, it was possible to determine the redshift using an instantaneous UVOT-XRT Spectral Energy Distribution (SED), which was created using the method of Schady et al. (2008). The SEDs were fit with the best fitting model of either a power-law or broken power-law, with Galactic and host galaxy absorption and extinction. The Galactic  $N_H$  was taken from the Leiden/Argentine/Bonn (LAB) Survey of Galactic HI (Kalberla et al. 2005) and the Galactic extinction was taken from a composite 100 $\mu$ m map of COBE/DIRBE and IRAS/ISSA observations (Schlegel et al. 1998). For the host extinction the Small Magellanic Cloud (SMC) extinction curve (Pei 1992) was assumed. The host reddening and absorption,  $E(B-V)$ ,  $N_H$ , and the redshift were left to vary. The resulting redshifts can be found in Table 2.

### 3.3 Luminosity Lightcurve

Luminosity lightcurves were produced for all the GRBs whose host  $E(B-V)$  value could be determined, except for GRBs with photometric redshifts which have a  $1\sigma$  error on the redshift that corresponds to an uncertainty in log luminosity of  $> 0.1$ . In total, luminosity lightcurves were produced for 21 of the GRBs in the sample.

For the 21 GRBs, the observed count rate was converted

<sup>1</sup> [http://heasarc.nasa.gov/docs/swift/analysis/UVOT\\_swguide\\_v2.2.pdf](http://heasarc.nasa.gov/docs/swift/analysis/UVOT_swguide_v2.2.pdf)

into luminosity at a common rest frame wavelength. In order to select the common wavelength and determine the resulting k-correction factor for each lightcurve, an SED was computed for each GRB. The SED was produced by multiplying the relative count rates in each filter, given in Table 1, by the count rate-to-flux conversion factors given by Poole et al. (2008). These relative flux densities were corrected for Galactic extinction and positioned at the central wavelength of the filter in the rest frame of the GRB; the SEDs are shown in Fig. 1. The common rest frame wavelength at which to determine the luminosities was selected to maximise the number of GRBs with SEDs that include this wavelength and to be relatively unaffected by host extinction. The wavelength which best satisfies these conditions is 1600Å. The k-correction factor was taken as the flux density in the rest frame at 1600Å,  $F_{1600}$ , divided by the flux density at the observed central wavelength of the v filter (5402Å),  $F_v$ . In the case where a GRB's SED did not cover 1600Å, an average k-correction was determined from the other GRBs in the sample, whose SEDs covered both 1600Å and the rest frame wavelength corresponding to the v filter.

To produce the luminosities, the lightcurves in count rate were corrected for Galactic extinction, converted into flux density and then into luminosity using the following equation:

$$L(1600) = 4\pi D_L^2 F_v k \quad (1)$$

where  $L(1600)$  is the luminosity at a 1600Å,  $D_L$  is the luminosity distance,  $k = (1+z)(F_{1600}/F_v)$  is the k-correction factor, and  $z$  is the redshift of the GRB. Finally, the luminosity lightcurves were corrected for host extinction using the  $A_{1600}$  values given in Table 1. These values were determined for the GRBs, using the  $A_v$  values reported in Schady et al. (2008).

### 3.4 Bolometric Energy and GRB Classification

The k-corrected isotropic energy of the prompt gamma-ray emission  $E_{k,iso}$ , was calculated for each GRB with known redshift using Eq. 4 from Bloom et al. (2001). The energies were corrected to a rest frame bandpass of 0.1 keV to 10000 keV using one of three spectral templates: a power-law, cut-off power-law or Band function (Band et al. 1993). As Konus-Wind has a larger energy range than BAT, the spectral analysis of the prompt emission, observed by Konus-Wind, better represents the spectral behaviour. These results were taken from the literature. The spectra observed with Konus-Wind tend to be best fit by a cut-off power-law, therefore the spectral template chosen for the GRBs that were not observed with Konus-wind, with power-law spectra of photon index  $\Gamma > -2$  in the 15 keV - 150 keV energy range was a cut-off power-law with  $E_{peak}=162.2$  keV (D'Alessio et al. 2006). For the GRBs with a power-law spectrum with a photon index of  $\Gamma < -2$  in the 15 keV - 150 keV energy range, a Band function was used with  $\Gamma_1 = -0.99$  (D'Alessio et al. 2006) and  $E_{peak}=15$  keV. The resulting k-corrected energies can be found in Table 3.

The GRBs in this sample were classified into three categories depending on the ratio  $R$  of the fluence in the 25 keV - 50 keV and 50 - 100 keV BAT energy bands, which are given in Sakamoto et al. (2008). The categories and their respective ratios are: an X-ray flash (XRF) for  $R > 1.32$ ; an X-ray

rich GRB (XRR) for  $0.72 < R \leq 1.32$ ; or a classical GRB (C-GRB) for  $R \leq 0.72$ . Table 4 lists the GRBs with their classifications. In total, there are 12 C-GRBs, 13 XRR and 1 XRF, which is GRB 060512.

## 4 RESULTS

In this Section, the flux lightcurves in the observer frame and their properties shall be investigated first, then the luminosity lightcurves in the rest frame and their properties shall be examined.

### 4.1 Observer Frame Flux Lightcurves

The lightcurves, shown in Fig. 2, are ordered by peak magnitude from the brightest, GRB 061007, to the faintest, GRB 050712. Data points with signal to noise below 2 are shown as  $3\sigma$  upper limits. The peak magnitude was taken as the maximum magnitude in each binned lightcurve and is given in Table 4. A trend is observed in the figure, with the brightest GRBs decaying more quickly than the faintest GRBs. The lightcurves generally follow one of two types of behaviour. Either they rise to a peak within the first 1000s and then decay, or they decay from the beginning of the observations. There are 6 lightcurves that appear to rise to a peak between 200s to 1000s after the burst trigger. The peak times for the 6 GRBs were determined from a Gaussian fit to each lightcurve in log time. The fit was performed between the brightest data point and the data points on either side to the point at which the count rate is 60% of the peak value. The mean of these peak times is 397s. For the remaining GRBs, the beginning of the lightcurve was taken as the upper limit to the peak time and the mean of these upper limits is 132s.

To classify the behaviour of the lightcurves, two power-laws were fit to each lightcurve, covering the time ranges from the start of observations until 500s and from 500s until the end of the observations; the results are given in Table 4. A time of 500s was chosen as it ensures that the early power law fits are performed on at least 100s of each lightcurve and because the rising phase tends to occur during the first 500s.

A comparison of the temporal indices before and after 500s is shown in Fig. 3. The figure is divided into three groups of behaviour, which are: lightcurves which rise before 500s, lightcurves which decay more steeply after 500s and lightcurves which decay less steeply after 500s. Each of these groups contains a similar number of GRBs. From Fig. 3, there are 4 lightcurves that are clearly rising with an  $\alpha_{<500s}$  ranging from  $0.26 \pm 0.13$  (GRB 060605) to  $0.73 \pm 0.14$  (GRB 070420). A further 7 lightcurves are consistent with  $\alpha_{<500s} \sim 0$  or have large errors and thus it is not clear if these lightcurves are rising, constant or decaying before 500s. The remaining 15 lightcurves decay with temporal indices of between  $\alpha_{<500s} = -0.12 \pm 0.05$  (GRB 061121) and  $\alpha_{<500s} = -2.67 \pm 0.80$  (GRB 050726). After 500s, all the lightcurves decay with values of  $\alpha_{>500s}$  ranging from  $-0.50 \pm 0.05$  (GRB 050712) to  $-1.67 \pm 0.15$  (GRB 070420), except for GRB 050726 where, due to the poor signal to noise, it is not possible to tell if the lightcurve after 500s is rising or decaying.

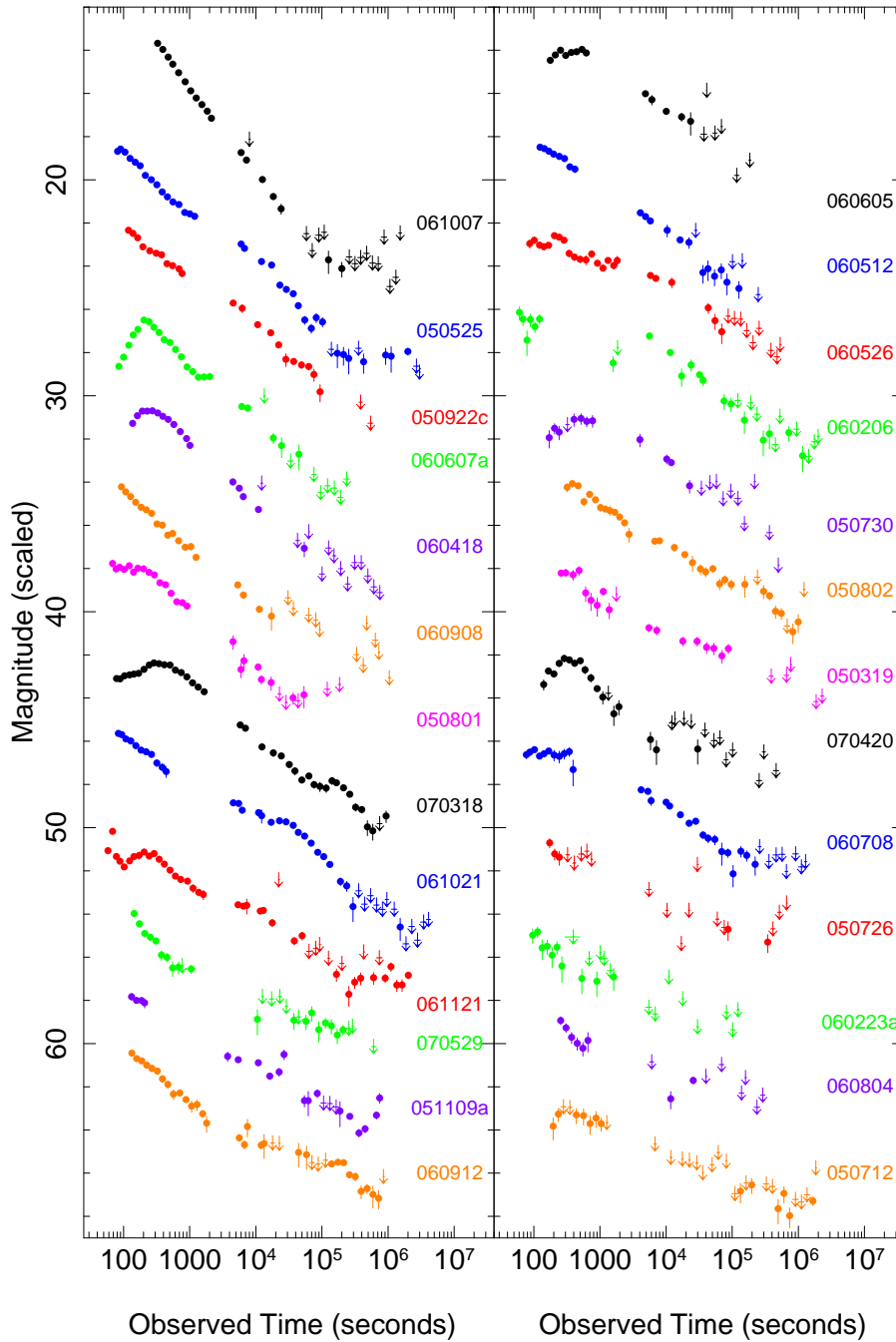


**Figure 2.** The lightcurves, ordered by peak magnitude from brightest (GRB 061007) to faintest (GRB 050712). With a few exceptions, the lightcurves appear also to be ordered by decay rate with the brighter bursts decaying more rapidly than the fainter bursts. The down arrows in each lightcurve represent  $3\sigma$  upper limits.

The mean and intrinsic dispersion of the temporal indices was determined using the maximum likelihood method (Maccacaro et al. 1988), which assumes a Gaussian distribution. The mean for  $\alpha_{<500s}$  is  $-0.48^{+0.15}_{-0.19}$  with a dispersion of  $0.69^{+0.19}_{-0.06}$  and the mean for  $\alpha_{>500s}$  is  $-0.88^{+0.08}_{-0.07}$  with a dispersion of  $0.31^{+0.07}_{-0.03}$ . To see if  $\alpha_{<500s}$  and  $\alpha_{>500s}$  are independent parameters, a Spearman rank test was performed. This test gives a coefficient of -0.22 with a probability of 73%, indicating no evidence for a correlation and suggest-

ing that the behaviour after 500s is independent of the behaviour before 500s.

Since the lightcurves in Fig. 2 suggest a connection between the brightness and the decay rate, a Spearman rank correlation was performed between the temporal indices and the interpolated magnitudes of the lightcurves at 400s. The test performed between  $\alpha_{<500s}$  and the magnitude at 400s, indicates that these parameters are not related, as the coefficient is -0.28 at 84% confidence. However, the Spearman rank test performed on  $\alpha_{>500s}$  and the magnitude at 400s

GRB	Redshift	$A_{1600}$	Count Rate Relative to v					white
			b	u	w1	m2	w2	
050319	3.24 <sup>a</sup>	0.27	1.36	-	-	-	-	N/A
050525	0.606 <sup>b</sup>	0.25	2.29	2.72	1.05	0.46	0.56	4.59
050712	-	-	-	0.68	-	-	-	N/A
050726	-	-	0.63	-	-	-	-	N/A
050730	3.97 <sup>c</sup>	0.64	0.78	-	-	-	-	N/A
050801	1.38 <sup>*</sup>	0.00	2.25	2.46	0.81	0.29	0.13	N/A
050802	1.71 <sup>d</sup>	0.47	2.75	2.34	0.52	0.05	0.07	4.79
050922c	2.198 <sup>e</sup>	0.35	1.99	1.83	0.11	-	-	N/A
051109a	2.346 <sup>f</sup>	0.04	1.98	0.88	0.21	-	-	7.96
060206	4.04795 <sup>g</sup>	0.00	0.42	-	-	-	-	N/A
060223a	4.41 <sup>h</sup>	-	0.26	-	-	-	-	4.18
060418	1.4901 <sup>i</sup>	0.34	1.82	1.40	0.36	0.07	0.06	6.21
060512	0.4428 <sup>j</sup>	1.93	3.03	2.31	0.20	-	-	8.46
060526	3.221 <sup>k</sup>	0.00	1.39	-	-	-	-	2.99
060605	3.8 <sup>l</sup>	1.08	0.79	-	-	-	-	2.74
060607a	3.082 <sup>m</sup>	0.21	1.56	0.19	-	-	-	4.36
060708	1.92 <sup>*</sup>	0.56	1.85	1.76	0.25	-	-	7.49
060804	-	-	2.10	0.00	-	-	-	N/A
060908	2.43 <sup>n</sup>	0.08	2.07	2.23	0.40	-	-	9.27
060912	0.937 <sup>o</sup>	2.09	1.58	2.16	0.41	0.17	0.27	8.83
061007	1.262 <sup>p</sup>	2.77	1.84	1.35	0.25	0.07	0.06	6.03
061021	0.77 <sup>*</sup>	0.00	2.38	3.14	1.74	0.81	1.23	11.97
061121	1.314 <sup>q</sup>	1.35	2.70	2.45	0.58	0.17	0.14	9.03
070318	0.836 <sup>r</sup>	1.72	1.75	1.50	0.29	0.08	0.07	6.69
070420	3.01 <sup>*</sup>	1.53	1.52	0.47	0.19	-	-	6.35
070529	2.4996 <sup>s</sup>	0.57	3.42	0.92	-	-	-	N/A

**Table 1.** Spectroscopic redshifts were largely taken from the literature. For four GRBs, photometric redshifts, indicated by an \*, were determined using the XRT-UVOT SEDs (see Section 3 for more details). The host extinction values at 1600Å, were calculated from the best fit  $A_v$  given in (Schady et al. 2008). The count rate relative to v is provided for each filter detected by the UVOT. For a few GRBs, there were no observations with the white filter and for GRB 060804, the white data could not be used; the white column for these GRBs contain N/A. References: a) Jakobsson et al. (2006a) b) Foley et al. (2005) c) Chen et al. (2005) d) Fynbo et al. (2005) e) Jakobsson et al. (2006a) f) Quimby et al. (2005) g) Fynbo et al. (2006) h) Berger et al. (2006) i) Prochaska et al. (2006) j) Bloom et al. (2006) k) Jakobsson et al. (2006a) l) Peterson & Schmidt (2006) m) Ledoux et al. (2006) n) Rol et al. (2006) o) Jakobsson et al. (2006) p) Jakobsson et al. (2006) q) Bloom et al. (2006) r) Jaunsen et al. (2007) s) Berger et al. (2007)

gives a coefficient of 0.59 at 99.8% confidence (see Fig. 4). The correlation is statistically significant at  $> 3\sigma$  and therefore implies that brighter GRBs tend to have faster decays.

The mean redshifts of the two columns in Fig. 2 are  $\langle z \rangle = 1.63$  and  $\langle z \rangle = 2.98$ , suggesting that the decay rate and magnitude are also correlated with redshift because the optical afterglows that are brighter and decay more steeply tend to have lower redshifts. A Spearman Rank test performed between  $\alpha_{>500s}$  and redshift gives no evidence for a correlation with a correlation coefficient of 0.07 and a insignificant probability of 23%. However, a Spearman Rank test performed between the redshift and magnitude at 400s, provides a weak correlation with a coefficient of 0.32 and a statistical significance of 87%. Moreover, if the Spearman Rank test is performed between the peak magnitude and redshift, the link between the redshift and magnitude is stronger and more significant as the coefficient is 0.55 and the confidence is 99.3%. These correlations imply that the correlation between magnitude at 400s and  $\alpha_{>500s}$  is only weakly dependent on redshift.

The lightcurves of the GRBs after 500s, in a few cases, appear to show a change in their temporal behaviour. To quantify this behaviour, a broken power-law was fitted to each GRB from 500s until the end of the observations. The broken power-law is considered an improvement if the  $\chi^2/D.O.F$  has decreased and the probability of chance improvement is small ( $< 1\%$ ), as determined using an F-test. In five cases a broken power-law was an improvement compared with a single power-law. The results of the broken power-law fits for the 5 GRBs are given in Table 5. In four of these five cases, the broken power-law shows a transition from a shallow to a steeper decay. In the fifth case, GRB 070318, the decay became shallower at late times. To test if a single break is sufficient for the decay after

GRB	Photometric Redshift	$\chi^2/D.O.F$
GRB050801	$1.38 \pm 0.07$	(14/12)
GRB060708	$1.92 \pm 0.12$	(21/20)
GRB061021	$0.77^{+0.06}_{-0.01}$	(229/174)
GRB070420	$3.01^{+0.96}_{-0.68}$	(58/60)

**Table 2.** Photometric redshifts for 4 of the GRBs without spectroscopic redshifts.

500s, a doubly broken power-law was fit to these 5 GRBs. As with the broken power-law, the doubly broken power-law was considered an improvement if the  $\chi^2/D.O.F$  decreased and the probability of chance improvement is small ( $< 1\%$ ). The doubly broken power-law was an improvement for only GRB 070318. The best fit values for this model are:  $\alpha_1 = -1.08 \pm 0.01$ ,  $t_{break,1} = 53800^{+6800}_{-6100}$ ,  $\alpha_2 = -0.11^{+0.12}_{-0.14}$ ,  $t_{break,2} = 197000^{+22000}_{-15000}$ ,  $\alpha_3 = -1.72 \pm 0.18$  with  $\chi^2/D.O.F = 62/23$ .

For the 4 GRBs where the broken power-law was the best fit, the mean decay index before the break is  $-0.60 \pm 0.14$  with a dispersion of  $0.19^{+0.18}_{-0.07}$  and the mean decay index after the break is  $-1.53 \pm 0.19$  with a dispersion of  $0.22^{+0.28}_{-0.09}$ . The break times range from  $6000^{+1000}_{-1100}$  s to  $(4.9 \pm 0.25) \times 10^4$  s. If the mean decay index after 500s is recalculated including only those lightcurves that decay as a single power-law after 500s, the mean is  $-0.87^{+0.10}_{-0.09}$  with a dispersion of  $0.35^{+0.10}_{-0.04}$ . This mean is similar to the mean decay index determined using all the GRBs in the sample. For the lightcurves that show a break, the mean decay before the break is consistent within  $2\sigma$  with these mean values.

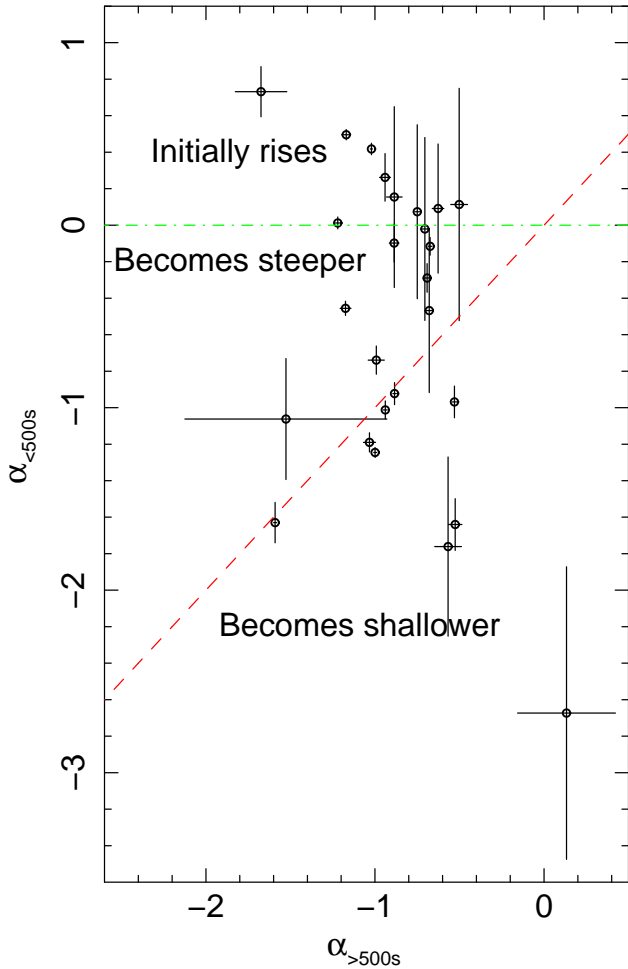


**Figure 3.** Temporal decay after 500s versus temporal decay before 500s. The dashed (red) line indicates the point at which the temporal index before 500s equals the temporal index after 500s. The dashed dotted (green) line indicates the cut off between GRBs that rise within the first 500s (above the line) and GRBs that decay within the first 500s (below the line).

## 4.2 GRB Rest Frame Luminosity Lightcurves

The luminosity lightcurves at  $1600\text{\AA}$ , in units of  $\text{erg s}^{-1} \text{cm}^{-1} \text{\AA}^{-1}$ , before and after correction for host extinction, are shown in Fig. 5. Panel (a) shows the luminosity lightcurves before any correction for the host extinction has been applied. In both panels of Fig. 5, GRB 060512 lies significantly below all the other lightcurves. We suspect that this is caused by either an incorrect determination of the host extinction or of the redshift. The redshift of this GRB could be wrong because it was not determined from the afterglow spectra, but was based on the alignment of the GRB with a galaxy (Bloom et al. 2006). In Schady et al. (2008), the best fitting model to the SED of GRB 060512 gives a poor fit with a  $\chi^2/D.O.F = 84/23$  and a host extinction of  $E(B-V)_{\text{host}} = 0.16^{+0.01}_{-0.00}$ . A photometric redshift was determined for this GRB using the method described in Section 2, of  $z = 2.279^{+0.09}_{-0.18}$  and an extinction of  $A_{1600} = 0.00^{+0.02}_{-0.00}$ . Using these values a luminosity lightcurve for GRB 060512 at  $1600\text{\AA}$  was produced. This photometric redshift changes the rest frame relative flux SED and consequently the k-

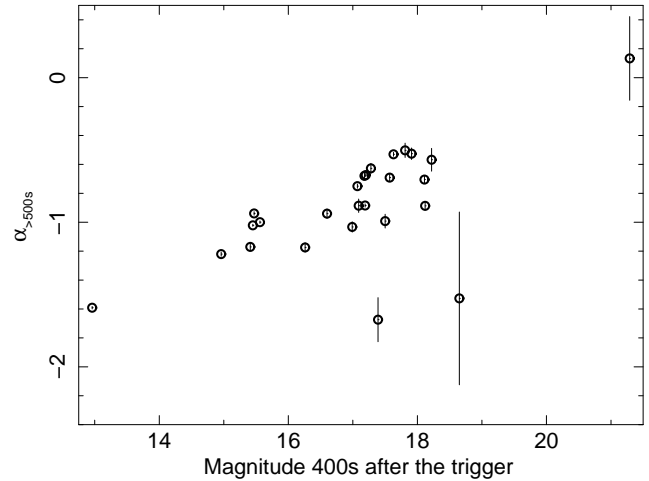


**Figure 4.** Magnitude at 400s against the temporal index after 500s,  $\alpha_{>500s}$ . A Spearman rank correlation test performed on these parameters gives a coefficient of 0.59 at a statistical significance of 99.8%, indicating that these two parameters are correlated.

GRB		$D_L$ (cm)	$\beta_1$	$\beta_2$	$E_{\text{peak}}$	$E_{\text{iso},k}$
050319	BAND	$8.60 \times 10^{28}$	-0.99	-2.02 <sup>a</sup>	162.0	1.44e+53
050525	CPL	$1.10 \times 10^{28}$	-1.10 <sup>b</sup>	-2.31	84.1 <sup>b</sup>	1.59e+53
050730	CPL	$1.04 \times 10^{29}$	-1.53 <sup>a</sup>	-2.31	162.2	3.85e+54
050801	CPL	$3.04 \times 10^{28}$	-1.99 <sup>a</sup>	-2.31	162.2	7.67e+53
050802	CPL	$3.96 \times 10^{28}$	-1.54 <sup>a</sup>	-2.31	162.2	5.86e+53
050922c	CPL	$5.38 \times 10^{28}$	-1.55 <sup>c</sup>	-2.31	162.2	4.30e+54
051109a	CPL	$5.82 \times 10^{28}$	-1.25 <sup>d</sup>	-2.31	161.0 <sup>d</sup>	6.43e+53
060206	CPL	$1.12 \times 10^{29}$	-1.20 <sup>a</sup>	-2.31	78.0 <sup>a</sup>	3.42e+53
060223a	CPL	$1.24 \times 10^{29}$	-1.74 <sup>a</sup>	-2.31	162.2	4.47e+54
060418	CPL	$3.34 \times 10^{28}$	-1.50 <sup>e</sup>	-2.31	230.0 <sup>e</sup>	2.94e+54
060512	BAND	$7.56 \times 10^{27}$	-0.99	-2.48 <sup>a</sup>	162.2	5.04e+50
060526	BAND	$8.54 \times 10^{28}$	-0.99	-2.01 <sup>a</sup>	162.2	1.37e+53
060605	CPL	$1.04 \times 10^{29}$	-1.55 <sup>a</sup>	-2.31	162.2	1.15e+54
060607a	CPL	$8.10 \times 10^{28}$	-1.47 <sup>a</sup>	-2.31	162.2	1.81e+54
060708	CPL	$4.56 \times 10^{28}$	-1.68 <sup>a</sup>	-2.31	162.2	3.79e+53
060908	CPL	$6.08 \times 10^{28}$	-1.00 <sup>a</sup>	-2.31	151.0 <sup>a</sup>	1.88e+53
060912	POWER	$1.88 \times 10^{28}$	-1.74 <sup>f</sup>	-2.31	162.2	2.52e+54
061007	BAND	$2.72 \times 10^{28}$	-0.70 <sup>g</sup>	-2.61 <sup>g</sup>	399.0 <sup>g</sup>	2.00e+53
061021	CPL	$1.48 \times 10^{28}$	-1.22 <sup>h</sup>	-2.31	777.0 <sup>h</sup>	9.65e+52
061121	CPL	$2.86 \times 10^{28}$	-1.32 <sup>i</sup>	-2.31	606.0 <sup>i</sup>	2.75e+54
070318	CPL	$1.63 \times 10^{28}$	-1.42 <sup>a</sup>	-2.31	162.2	8.78e+52
070420	CPL	$7.87 \times 10^{28}$	-1.23 <sup>j</sup>	-2.31	147.0 <sup>j</sup>	6.39e+54
070529	CPL	$6.14 \times 10^{28}$	-1.34 <sup>a</sup>	-2.31	162.2	6.46e+53

**Table 3.** Properties of the GRBs with spectroscopic or photometric redshifts. This table contains the luminosity distance, the gamma-ray photon indices and peak energies used to determine the k-corrected isotropic energy for each GRB in the energy range 10 keV - 10 MeV. References: a) Sakamoto et al. (2008), b) Golenetskii et al. (2005a), c) Golenetskii et al. (2005b) d) Golenetskii et al. (2005c), e) Golenetskii et al. (2006), f) Golenetskii et al. (2006b), g) Golenetskii et al. (2006c), h) Golenetskii et al. (2006d), i) Golenetskii et al. (2006a), j) Golenetskii et al. (2007)

correction factor. The result is that the luminosity lightcurve increases by  $\sim 3$  orders of magnitude, which means that this GRB is no longer separated from the rest of the GRBs in the sample. Nonetheless, this GRB may be intrinsically different to all the other GRBs in the sample as this GRB is the only XRF in the sample and it may be that XRFs are a class of sub-luminous GRBs. However, as it is uncertain whether the redshift of GRB 060512 is correct, the luminosity lightcurve for this GRB will be excluded from any further analysis.

To produce luminosity distributions, the luminosities were interpolated from the lightcurves before and after correction for host extinction at the 3 rest frame epochs: 100s, 1000s and 10 ks. The logarithmic distribution of the luminosities at the three epochs are shown in Panels (a) to (f) of Fig. 6. The distributions consisting of the luminosities at 100s contain 18 GRBs whereas the distributions for the luminosities at 1000s and 10 ks contain 20 GRBs. Panels (a) to (c), show the logarithmic distribution of luminosities before correction for host extinction. The means of these distributions at 100s, 1000s and 10 ks in the rest frame are 11.08, 10.29 and 9.39, respectively. The standard deviations at the three rest frame epochs are 0.65 at 100s, 0.71 at 1000s, and 0.68 at 10 ks. Panels (d) to (f) show the logarithmic distributions of the luminosity lightcurves that have been corrected for host extinction. The mean of the host extinction corrected distributions at 100s, 1000s and 10 ks in the rest frame are 11.29, 10.55 and 9.64, respectively and the standard deviations are 0.57 at 100s, 0.67 at 1000s, and 0.62 at 10 ks.

The distribution of rest frame peak times and upper limits is shown in Fig. 7. The peak times of the GRBs with observed peaks overlap with the upper limits of the GRBs without observed peaks. Therefore, it is not possible to tell if the GRBs with observed peaks are a separate class, or if they belong to the tail end of a distribution where the majority of GRB peaks occur before the UVOT can observe them.

To determine if the relationship between the brightness of the afterglow and the late time decay rate is intrinsic, the luminosity lightcurves were fitted with a power-law from 150s onwards  $\alpha_{>150s,rest}$ , where  $150s \simeq 500s/(1 + \langle z \rangle)$  and  $\langle z \rangle = 2.21$  is the mean redshift of the GRBs in the sample, and a Spearman rank test was performed between this decay and the extinction corrected luminosity at 100s in the rest frame. These parameters are shown in Fig. 8. The Spearman rank test does not support or refute a correlation between these parameters because the coefficient is -0.29 and the probability of correlation is not significant at 76%.

## 5 DISCUSSION

In this section, we shall discuss the possible mechanisms that could produce the rising behaviour of the early afterglow viewed in the observer frame before 500s, and we shall discuss the late afterglow from 500s onwards. We will also discuss the implications of the luminosity distribution and compare the UVOT lightcurves with the XRT canonical lightcurve model.

### 5.1 The early UVOT afterglow

There are several physical mechanisms and geometric scenarios that may produce a rise in the early optical afterglow. In this section the following mechanisms and scenarios shall be discussed: (i) passage of the peak synchrotron frequency of the forward shock  $\nu_{m,f}$ , through the observing band, (ii) a reverse shock, (iii) decreasing extinction with time, (iv) the onset of the forward shock in the cases of an isotropic outflow or a jet viewed in a region of uniform energy den-

GRB	Lorentz Factor at Peak	$M_{fb}$	$R_{dec}$
050319	>168	<2.40e-04	<9.33e+16
050525	>179	<2.49e-04	<9.25e+16
050730	174	6.18e-03	2.72e+17
050801	>275	<7.81e-04	<1.17e+17
050802	>156	<1.05e-03	<1.56e+17
050922c	>308	<3.91e-03	<1.93e+17
051109a	>236	<7.61e-04	<1.22e+17
060206	>338	<2.83e-04	<7.80e+16
060223a	>409	<3.06e-03	<1.62e+17
060418	193	4.27e-03	2.32e+17
060512	> 72	<1.95e-06	<2.48e+16
060526	>247	<1.55e-04	<7.09e+16
060605	177	1.82e-03	1.80e+17
060607a	220	2.30e-03	1.81e+17
060708	>256	<4.14e-04	<9.72e+16
060908	>231	<2.27e-04	<8.23e+16
060912	>235	<3.00e-03	<1.94e+17
061007	>126	<4.42e-04	<1.26e+17
061021	>173	<1.56e-04	<7.99e+16
061121	>337	<2.28e-03	<1.57e+17
070318	103	2.38e-04	1.09e+17
070420	228	7.84e-03	2.69e+17
070529	>234	<7.71e-04	<1.23e+17

**Table 6.** Properties of the GRBs, derived assuming the rise of the forward shock is the cause of the rise observed in the UVOT lightcurves. The initial Lorentz factors were determined using the peak times and Eq. 1 of Molinari et al. (2007). Where only an upper limit to the peak time is known, only a lower limit to the Lorentz factor is given. The fraction of mass as baryons and the deceleration radius are determined using the Lorentz factor.

sity, (v) the rise produced by an off-axis jet, which may be structured, and finally, (vi) a two component outflow.

#### 5.1.1 Passage of the synchrotron frequency, $\nu_{m,f}$

The first mechanism, the passage of the peak frequency of the forward shock which moves with time as  $\nu_{m,f} \propto t^{-3/2}$ , through the observing band is expected to produce a chromatic peak in the optical lightcurve evolving from the shortest wavelengths through to the longest wavelengths. For 5 of the lightcurves with a peak, the UVOT observed the majority of the rise and the peak during the two finding chart exposures observed in white and v (see Fig. 9). If the peak were due to the passage of the synchrotron frequency, a stepped decrease in flux would be observed in the normalized lightcurves at the transition between the white and v observations, which has not been observed in any of these GRBs. For the 6th GRB with an observed peak, GRB 050730, the rise was observed in the v and b filters. If the passage of  $\nu_{m,f}$  was the cause of this rise, the afterglow would appear to be brighter in the b filter than in the v filter during the rise, and begin to decay earlier. However, the afterglow is not brighter in the b filter than in the v filter during the rise. Therefore, the passage of  $\nu_{m,f}$  through the optical band is not responsible for any of the peaks observed in these optical afterglows.

During the passage of  $\nu_m$  from the shortest wavelengths through to the longest wavelengths, the spectrum of the optical afterglow changes (assuming slow cooling) from  $\nu^{1/3}$ , for  $\nu < \nu_m$  to  $\nu^{-(p-1)/2}$ , for  $\nu_m < \nu < \nu_c$  (Sari et al. 1998). As  $\nu_m$  passes from high frequencies to lower frequencies, there will be a change in colour. The colour change between the white and v filters can be calculated using the central wavelengths of the white and v filters, given in Poole et al. (2008), converted in to frequency:  $\nu_{white} = 8.64 \times 10^{14}$  Hz,  $\nu_v = 5.49 \times 10^{14}$  Hz and assuming  $p = 2.3$  where  $p$  is the electron energy index. The colour change between white and v as  $\nu_m$  moves from above the white frequency to below the

Name	Classification	Peak Magnitude	Peak Time (s)	$\alpha_{<500s}$	( $\chi^2/D.O.F$ )	$\alpha_{>500s}$	( $\chi^2/D.O.F$ )
050319	XRR	17.09	< 234	$0.09 \pm 0.35$	0/ 2	$-0.63 \pm 0.03$	34/17
050525	XRR	13.57	< 78	$-1.25 \pm 0.03$	21/ 9	$-1.00 \pm 0.01$	398/26
050712	C-GRB	17.77	< 178	$0.11 \pm 0.64$	4/ 3	$-0.50 \pm 0.05$	52/26
050726	C-GRB	17.21	< 159	$-2.67 \pm 0.80$	1/ 3	$0.13 \pm 0.29$	21/13
050730	C-GRB	17.22	744	$0.15 \pm 0.50$	6/ 3	$-0.89 \pm 0.05$	72/16
050801	XRR	15.26	< 66	$-0.46 \pm 0.04$	43/10	$-1.17 \pm 0.03$	41/15
050802	XRR	17.07	< 289	$0.07 \pm 0.48$	0/ 1	$-0.75 \pm 0.01$	53/29
050922c	C-GRB	14.34	< 109	$-1.01 \pm 0.05$	21/ 6	$-0.94 \pm 0.01$	88/14
051109a	C-GRB	16.33	< 122	$-0.47 \pm 0.45$	0/ 2	$-0.68 \pm 0.02$	80/16
060206	XRR	16.64	< 57	$-0.02 \pm 0.50$	9/ 4	$-0.70 \pm 0.03$	205/22
060223a	XRR	17.33	< 88	$-1.06 \pm 0.33$	4/ 6	$-1.53 \pm 0.60$	31/14
060418	XRR	14.69	260	$0.01 \pm 0.03$	138/ 6	$-1.22 \pm 0.01$	58/21
060512	XRF	16.50	< 114	$-0.74 \pm 0.08$	3/ 6	$-0.99 \pm 0.05$	10/14
060526	XRR	16.59	< 82	$-0.29 \pm 0.08$	36/ 8	$-0.69 \pm 0.02$	141/22
060605	XRR	16.50	459	$0.26 \pm 0.13$	6/ 4	$-0.94 \pm 0.03$	27/11
060607a	C-GRB	14.50	254	$0.50 \pm 0.03$	702/ 8	$-1.17 \pm 0.03$	152/20
060708	XRR	17.19	< 72	$-0.10 \pm 0.10$	8/ 9	$-0.89 \pm 0.03$	39/23
060804	XRR	17.43	< 231	$-1.76 \pm 0.49$	0/2	$-0.57 \pm 0.08$	21/9
060908	C-GRB	15.21	< 88	$-1.19 \pm 0.05$	6/ 8	$-1.03 \pm 0.04$	20/18
060912	XRR	16.44	< 114	$-0.97 \pm 0.09$	2/ 6	$-0.53 \pm 0.01$	149/27
061007	C-GRB	12.68	< 298	$-1.63 \pm 0.11$	1/ 1	$-1.59 \pm 0.01$	129/28
061021	C-GRB	15.64	< 79	$-0.92 \pm 0.06$	3/ 9	$-0.88 \pm 0.01$	556/29
061121	C-GRB	15.67	< 53	$-0.12 \pm 0.05$	181/11	$-0.67 \pm 0.01$	179/31
070318	C-GRB	15.37	316	$0.42 \pm 0.03$	19/ 9	$-1.02 \pm 0.01$	261/27
070420	C-GRB	17.16	347	$0.73 \pm 0.14$	13/ 5	$-1.67 \pm 0.15$	56/23
070529	C-GRB	15.95	< 131	$-1.64 \pm 0.14$	5/ 5	$-0.53 \pm 0.04$	42/19

**Table 4.** The  $v$  peak magnitude, peak time and best fit decay indices of the lightcurves before and after 500s and the classification of each GRB. In the cases where a peak was not observed an upper limit to the peak time is provided. The GRBs are classified into three categories depending on the ratio of the fluence in the 25 keV - 50 keV and 50 - 100 keV BAT energy bands, which are given in Sakamoto et al. (2008): an X-ray flash (XRF), an X-ray rich GRB (XRR) or a classical GRB (C-GRB).

GRB	$\alpha_1$	Break Time	$\alpha_2$	( $\chi^2/D.O.F$ )	$\Delta\chi^2$
GRB 050525	$-0.80 \pm 0.01$	$16400^{+1200}_{-1400}$	$-1.70 \pm 0.08$	( 120/24 )	278
GRB 050922c	$-0.76 \pm 0.03$	$6000^{+1100}_{-1000}$	$-1.20 \pm 0.05$	( 16/12 )	59
GRB 060526	$-0.33 \pm 0.04$	$30800^{+4700}_{-5800}$	$-2.33^{+0.65}_{-0.47}$	( 32/20 )	93
GRB 061021	$-0.51 \pm 0.02$	$49300^{+2500}_{-2500}$	$-1.60^{+0.07}_{-0.06}$	( 49/27 )	507
GRB 070318	$-1.09 \pm 0.01$	$16000^{+3600}_{-3000}$	$-0.78 \pm 0.03$	( 131/25 )	129

**Table 5.** Five of the lightcurves in the sample could be fit with a broken power-law from 500s onwards. The final column provides the difference in  $\chi^2$  (for 2 additional degrees of freedom) when fitting the lightcurve after 500s with a single and broken power laws.

$v$  frequency is 0.48 magnitudes. In the lightcurves of Fig. 9, which have been normalized using the late time data, the colour difference between the white and the  $v$  filter after the peak is zero. None of the 5 lightcurves, in Fig. 9, with early white and  $v$  observations, show such a large offset between the lightcurves in two filters during the rise. Furthermore, the equation for  $\nu_{m,f}$  in a constant density medium, as given by Zhang et al. (2006) as:

$$\nu_{m,f} = (6 \times 10^{15} Hz)(1+z)^{1/2} E_{52}^{1/2} \epsilon_e^2 \epsilon_B^{1/2} (t/1day)^{-3/2} \quad (2)$$

where  $E_{52} = 10^{52} E$  is the isotropic energy in units of  $10^{52}$  ergs,  $\epsilon_e$  is the fraction of energy in the electrons,  $\epsilon_B$  is the fraction of energy in the magnetic field,  $z$  is the redshift and  $t$  is the time. Assuming  $\epsilon_e$  and  $\epsilon_B$  are not evolving with time and given the time  $t_1$  at which  $\nu_{m,f}$  is at a given frequency  $\nu_1$ , the time  $t_2$  at which  $\nu_{m,f}$  is at the frequency  $\nu_2$  is given by:  $t_2 = t_1(\nu_2/\nu_1)^{-2/3}$ . Using the central wavelengths of the white and  $v$  filters, the  $v$  filter should peak  $1.35\times$  later than the white filter. There does not appear to be any time difference between the peak in the white and  $v$  filters in the 5 lightcurves shown in 9, therefore, the passage of  $\nu_m$  through the optical band is not the cause the rise in the optical band.

For  $\nu_{m,f}$ , to have passed below the  $v$  filter (5402Å) by the time the UVOT has begun observations ( $t \sim 100s$ ), using  $\langle E_{k,iso} \rangle = 1.5 \times 10^{54}$  erg and  $\langle z \rangle = 2.21$ , then  $\epsilon_e^2 \epsilon_B^{1/2} < 1.7 \times 10^{-5}$ . The values  $\epsilon_e$  and  $\epsilon_B$  provided in Panaitescu & Kumar (2002) for 10 GRBs give values for  $\epsilon_e^2 \epsilon_B^{1/2}$  ranging from  $3 \times$

$10^{-3}$  to  $2 \times 10^{-7}$ , suggesting that  $1.7 \times 10^{-5}$  is consistent with values found for other GRBs.

### 5.1.2 The reverse shock

Considering a constant density medium, there are two main cases of the reverse shock that depend on the position of the peak synchrotron frequency of the reverse shock  $\nu_{m,r}$  relative to the optical band  $\nu_{opt}$ . If  $\nu_{m,r} < \nu_{opt}$  then the lightcurve produced by the reverse shock is expected to decay immediately after the peak with  $\alpha = (3p + 1)/4$  (Zhang et al. 2003), where  $p$  is the electron energy index. The value of  $p$  is typically taken to lie between 2 and 3, therefore  $\alpha$  is expected to range between  $\alpha = -1.75$  for  $p = 2$  to  $\alpha = -2.5$  for  $p = 3$ . Within the sample, GRB 050726, GRB 061007 and GRB 070529 are the only GRBs with decays before 500s that are consistent at  $2\sigma$  with the slowest expected reverse shock decay index  $\alpha = -1.75$ ; GRB 050726 has a decay of  $\alpha = -2.67 \pm 0.80$ , GRB 061007 decays with  $\alpha = -1.63 \pm 0.11$  and GRB 070529 decays with  $\alpha = -1.64 \pm 0.14$ . The other lightcurves in the sample are shallower than the reverse shock prediction with  $> 2\sigma$  confidence. The second case arises if  $\nu_{m,r} > \nu_{opt}$ , then immediately after the peak there is an intermediate stage where  $\alpha \sim -0.5$ , which is followed by  $\alpha = (3p + 1)/4$ . In the sample, there are 7 GRBs that before 500s have temporal indices consistent with  $\alpha = -0.5$  at  $2\sigma$  confidence. However, of these GRBs only GRB 060223a has a decay after 500s

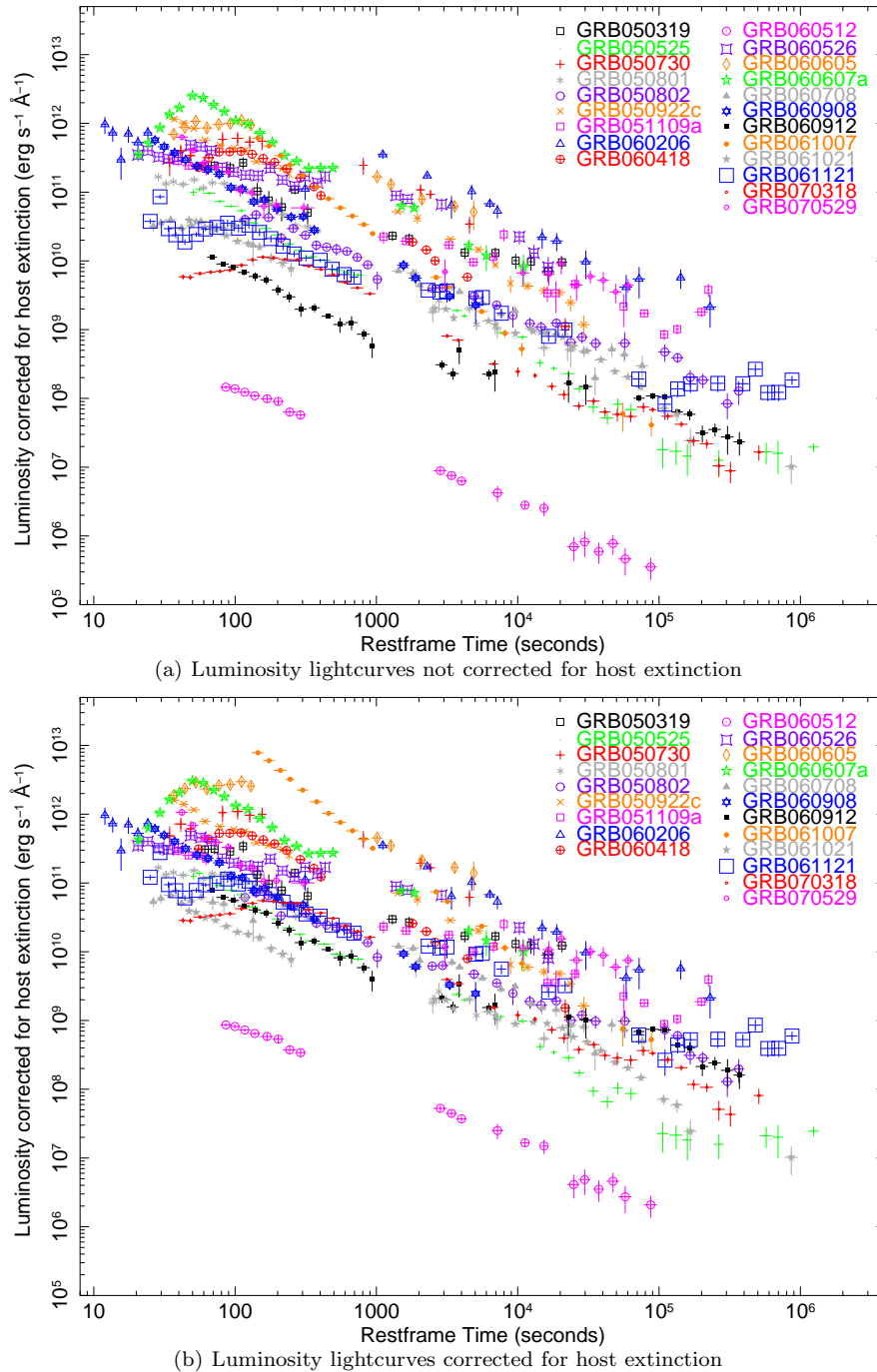


**Figure 5.** The luminosity lightcurves for the 21 lightcurves in the sample with spectroscopic or photometric redshifts. Panel A) shows the luminosity lightcurves before correction for the host extinction whereas Panel B) shows the luminosity lightcurves after correction for the host extinction. The grey lightcurves are the lightcurves with photometric redshifts.

( $\alpha = -1.53 \pm 0.60$ ) that is consistent at the  $2\sigma$  level with the slowest expected reverse shock decay index  $\alpha = -1.75$ .

The reverse shock in a wind medium is expected to produce a much steeper decay immediately after the peak with  $\alpha \sim -3.5$  (Kobayashi et al. 2004). Only GRB 050726, has a value of  $\alpha_{<500s}$ , which is consistent to within  $2\sigma$  confidence. All other GRBs are inconsistent at  $> 5\sigma$ .

The inconsistency of the temporal indices of the GRBs in this sample to the temporal decay expected during a re-

verse shock for both types of medium implies that the reverse shock is not the main contributor to the optical emission at early times, and therefore is not responsible for the rise. Still the reverse shock is expected to occur for all relativistic outflows that interact with the external medium. For a number of GRBs, the reverse shock may not be observed as it can be suppressed by high levels of magnetisation in the outflow (Zhang et al. 2006; Giannios et al. 2008) or if the forward and reverse shock have comparable energy, the

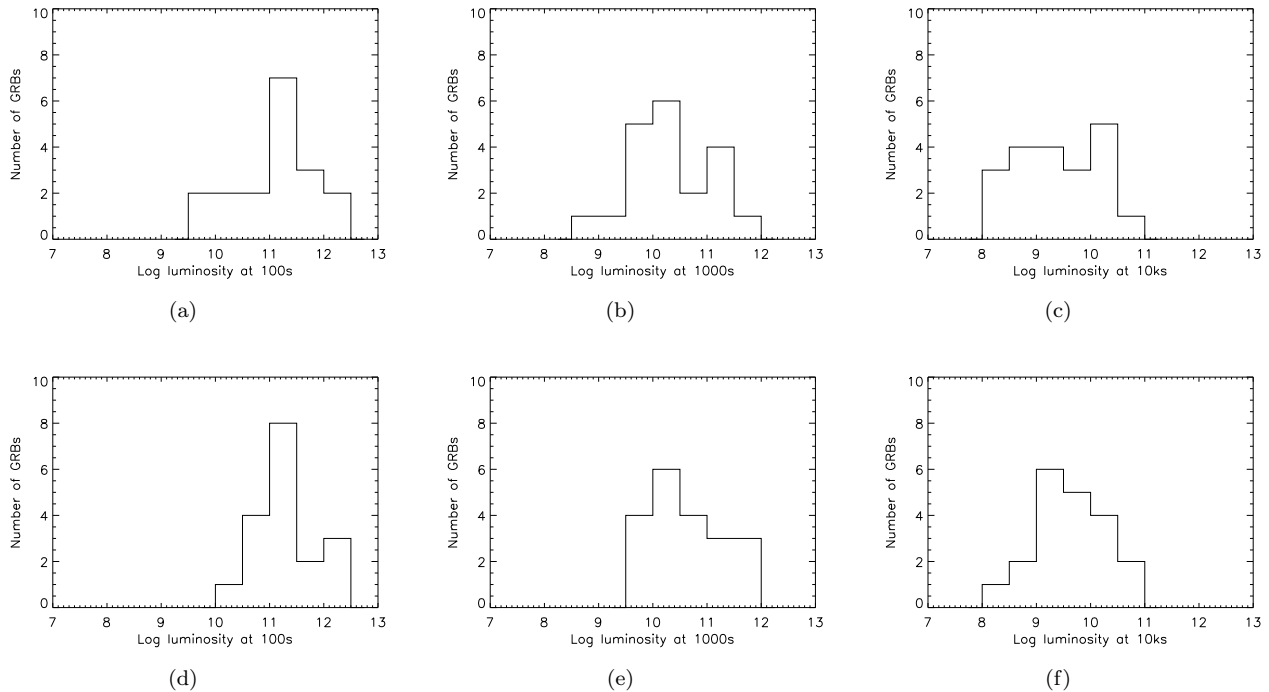


**Figure 6.** Luminosity Distributions. The luminosities in panels (a) to (c) show the luminosities at rest frame 100s, 1000s and 10 ks that have not been corrected for host extinction. Panels (d) to (f) show the luminosity distributions at the same epochs, but with the lightcurves corrected for host extinction.

sharp decay in the reverse shock may be masked by the flux produced by the forward shock (McMahon et al. 2006; Mundell et al. 2007).

### 5.1.3 Dust Destruction

If there are high levels of extinction at the beginning of the afterglow (Klotz et al. 2008, and references within), the lightcurve produced would be dim and reddened at the beginning. As the dust is destroyed by the radiation, a chromatic peak would be observed as the afterglow brightens and becomes less red. The bluer filters would be expected to rise more steeply when compared to the red filters as would the white filter, because the sensitivity of this filter is skewed to the blue. However, the amount of dust destroyed is highly dependent on the environment of the GRB, in particular to the density and the size of the region surrounding the progenitor, and simulations suggest that most of the dust destruction is expected to occur within the first few tens of seconds after the trigger (Perna & Lazzati 2002). Therefore, it is unlikely that the UVOT is observing the afterglow while dust destruction is occurring.

However, as the duration of dust destruction and the quantity of dust destroyed are only theoretical predictions, we must rule out dust destruction using observations. Therefore, the 6 UVOT lightcurves with a rise were examined to see if the bluer filters, including white, rise more steeply when compared to the  $v$  filter. The UVOT observed five of the lightcurves in white and  $v$  (the reddest UVOT filter) during the rise, see Fig. 9. GRB 060607a has the only lightcurve where there appears to be a significant excess in  $v$  compared with the white filter. However, the H band lightcurve given

in Molinari et al. (2007) rises at the same rate as the UVOT lightcurve, which was observing in white during the rise. If dust destruction was the cause of the rise, the H band would be expected to rise less steeply than the UVOT lightcurve. The 6th rising GRB, GRB 050730, was observed with the  $v$  and  $b$  filters during the rise and peak. If the peak in this case were due to dust destruction, an excess in  $v$  compared to  $b$  would be observed. However, the lightcurves of the  $v$  and  $b$  filters are consistent within  $1\sigma$  errors. Therefore, there is no evidence to suggest that dust destruction is the cause of the rise for this GRB or for any of the GRBs in this sample.

### 5.1.4 Start of the forward shock

At the start of the forward shock, a rise will be observed in the lightcurves as the jet ploughs into the external medium (Sari & Piran 1999). The lightcurves for an observer viewing within a uniform jet, or within a cone of uniform energy density will be the same as those observed within an isotropic outflow (Granot et al. 2002, and references within). The temporal index of the rise will vary according to the thickness of the shell and the density of the external medium. Assuming the synchrotron self absorption frequency  $\nu_a < \nu_{opt}$ , then the thickness of the shell and the density profile of the external medium affect the rate at which the lightcurve rises. For the thick shell case, the temporal index is  $\alpha = 1$  for a constant density medium, or  $\alpha = 1/9$  for a wind medium. For the thin shell case, in a constant density medium the temporal index is either  $\alpha = 2$  for  $\nu_c < \nu_{opt}$ , or  $\alpha = 3$  for  $\nu_c > \nu_{opt}$ . Lastly, the temporal index is  $\alpha = 0.5$  if the shell is thin and in a wind medium (Panaitescu & Vestrand 2008).

Given the peak time, the Lorentz factor  $\Gamma$  of the shell

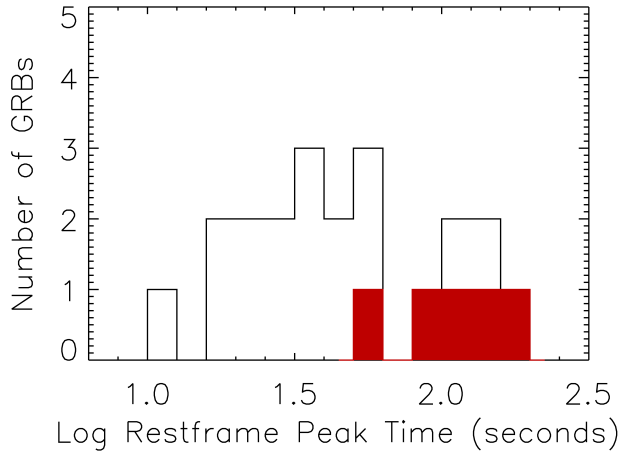


**Figure 7.** Distribution of the rest frame peak times. The red filled area represents the GRBs with known rest frame peak times, whereas the unfilled area contains the GRBs with known rest frame peak times and those GRBs with only upper limits to their peak time. Only 21 GRBs, for which luminosity lightcurves were produced, are included in this figure.

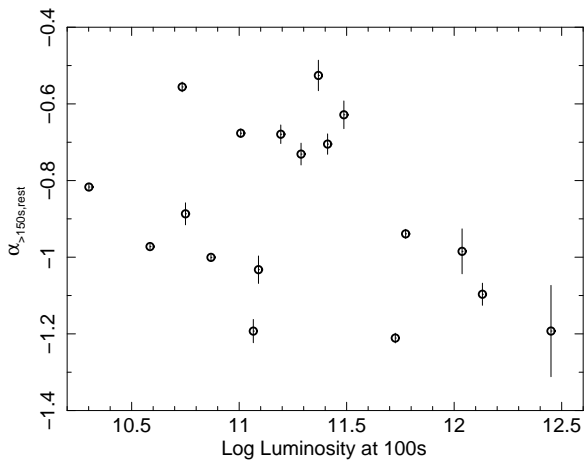


**Figure 8.** Temporal index determined from the lightcurves in the rest frame from 150s onwards, shown against luminosity of the lightcurves at 100s.

at the moment of the peak for a constant density medium, can be derived using the following equation (Molinari et al. 2007; Sari 1997):

$$\Gamma(t_{peak}) = \left( \frac{3E(1+z)^3}{32\pi n m_p c^5 \eta (t_{peak}/100s)^3} \right)^{1/8} \quad (3)$$

where  $t_{peak}$  is the peak time,  $\eta$  is the radiative efficiency and  $n$  is the density of the medium. Here we will assume  $\eta = 0.2$  and  $n = 1 \text{ cm}^{-3}$ . However, changing the values of  $\eta$  and  $n$  has a minor effect on the final values of  $\Gamma(t_{peak})$  as the dependence of  $\Gamma(t_{peak})$  on these parameters is small:  $\Gamma(t_{peak}) \propto (\eta n)^{-1/8}$ . For each GRB, the k-corrected energy, given in Table 3, was used in the equation above to determine  $\Gamma(t_{peak})$  and the resulting values of  $\Gamma(t_{peak})$  for the individual GRBs can be found in Table 3. The mean of the  $\Gamma(t_{peak})$  for the GRBs with a peak in their lightcurve is  $\langle \Gamma(t_{peak}) \rangle \sim 180$ , which is consistent with the expect-

tation that the initial Lorentz factor of the jet  $\Gamma_0$ , where  $\Gamma_0 \sim 2\Gamma(t_{peak})$  (Panaitescu & Kumar 2000; Meszaros 2006), of GRBs is  $> 100$  (Fenimore et al. 1993). For the GRBs where only an upper limit to their peak time is known, the mean value for  $\Gamma(t_{peak})$  is a lower limit,  $\langle \Gamma(t_{peak}) \rangle > 230$ . This suggests that the GRBs with observed peaks typically have lower Lorentz factors than the GRBs with upper limits to their peak times.

Using the derived values of  $\Gamma(t_{peak})$ , it is possible to deduce two more quantities: the isotropic-equivalent mass of the baryonic load  $M_{fb} = E/(\Gamma_0 c^2)$ , and the deceleration radius  $R_{dec} \simeq 2ct_{peak}\Gamma(t_{peak})^2/(1+z)$  (Molinari et al. 2007). These quantities were determined for each GRB and the results are given in Table 6. The mean mass of the baryonic load and the mean deceleration radius for the GRBs with an observed rise are  $\langle M_{fb} \rangle = 3.8 \times 10^{-3} M_\odot$  and  $\langle R_{dec} \rangle = 2.1 \times 10^{17} \text{ cm}$  and for the GRBs without an observed rise the quantities are  $\langle M_{fb} \rangle < 1.1 \times 10^{-3} M_\odot$  and  $\langle R_{dec} \rangle < 1.2 \times 10^{17} \text{ cm}$ . The deceleration radii are in agreement with  $R_{dec} \sim 10^{16} \text{ cm}$  as predicted by theory (Rees & Meszaros 1992). Therefore the forward shock is consistent with our observations.

### 5.1.5 Off-axis and structured outflows

A rise may be produced in the lightcurve if the observer's viewing angle is  $\theta_{obs} > \theta$ , where  $\theta_{obs}$  is the observer's viewing angle and  $\theta$  is the half opening angle of the jet. In the case of a uniform jet, the ejecta are released into a cone of angle  $\theta$  and due to relativistic effects, the emission in the jet is beamed as  $\Gamma^{-1}$ . If  $\theta_{obs} > \theta$ , then the emission is strongly beamed away from the observer, but as  $\Gamma$  decreases, the emission entering the line of sight increases and the observed lightcurve will rise. The lightcurve will peak when  $\Gamma \sim (\theta_{obs} - \theta)^{-1}$  (Granot et al. 2002). Larger observing angles will view a later peak and the peak magnitude will be lower (Granot et al. 2005). A structured jet, in which the energy per solid angle decreases around a uniform core of angular size  $\theta_c$ , viewed off-axis ( $\theta_{obs} > \theta_c$ ) can produce a rise in the optical afterglow, where the behaviour of the rise may vary depending on the distribution of energy around the core. In this case, the more diffuse the energy per solid angle the slower the rise and the later the peak time (Panaitescu & Vestrand 2008; Granot et al. 2002). The peak time of the lightcurve is also dependent on the viewing angle of the jet and the peak will occur when  $\Gamma \sim (\theta_{obs} - \theta_c)^{-1}$ .

### 5.1.6 Two Component Outflows

A two component outflow consists of a narrow jet surrounded by a wide jet. The narrow component will be denoted by a subscript  $n$  and the wide component will be denoted by a subscript  $w$ . Both components move at relativistic speeds, but the narrow jet will have a larger  $\Gamma$  (i.e.  $\Gamma_w < \Gamma_n$ ) and the wide component will have a larger half opening angle than the inner narrow jet (i.e.  $\theta_w < \theta_n$ ). The optical emission is expected to be produced either within the wide component (de Pasquale et al. 2008; Oates et al. 2007) or more traditionally from both the narrow and wide components (Peng et al. 2005; Huang et al. 2004).

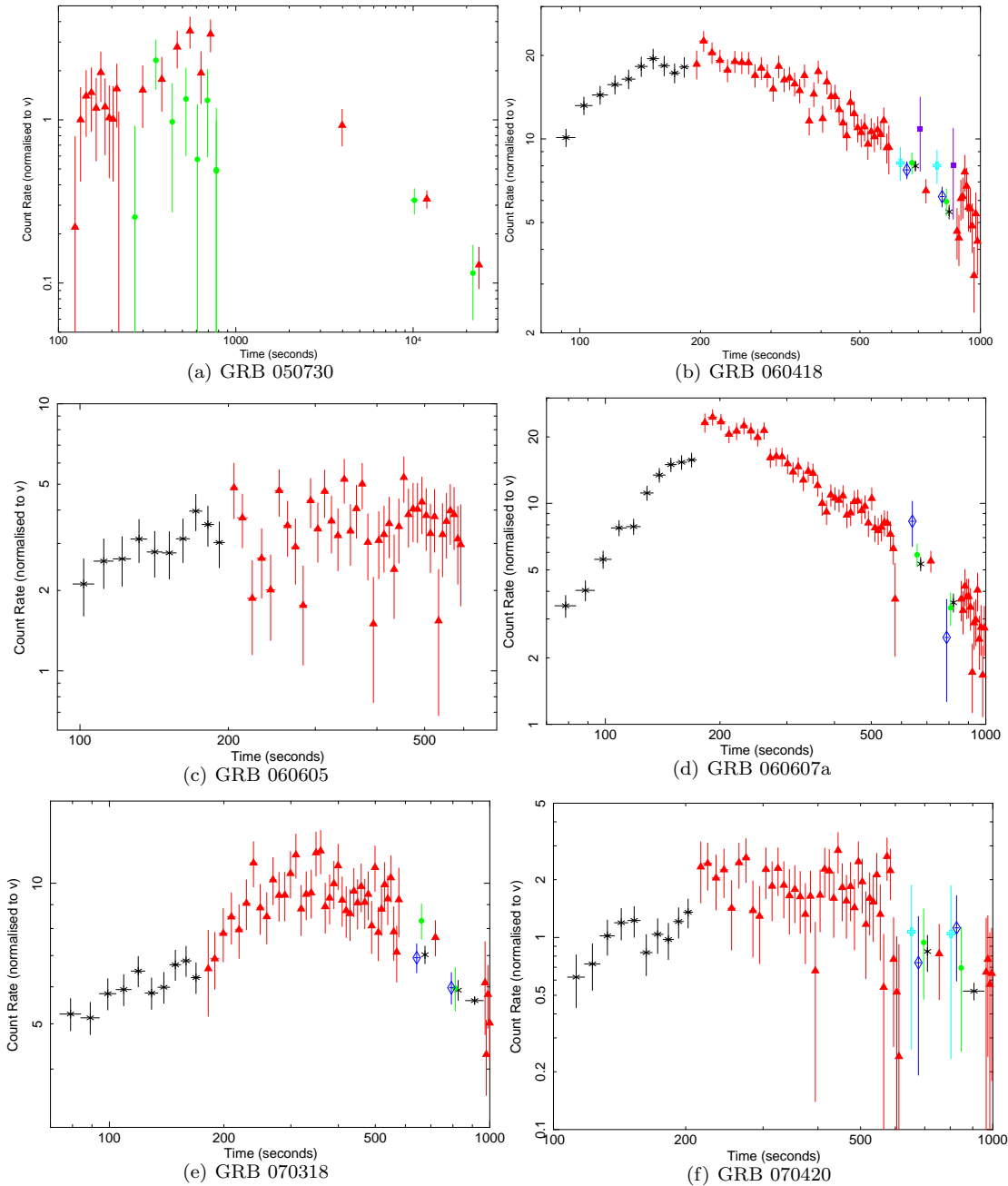


**Figure 9.** The early normalized lightcurves for the 6 GRBs with observed rises. GRB 050730 is the only GRB observed to rise that was not viewed with the white filter. Key: black star = white, red filled triangle = v, green circle = b, blue diamond = u, light blue cross = uvw1, pink hexagon = uvm2, purple square = uvw2

In the case where the optical emission is only produced by the wide component, the rise observed will occur as in Section 5.1.4, provided that the jet is viewed within  $1.5\theta_w$ , as has been demonstrated by Granot et al. (2002). At angles larger than  $1.5\theta_w$ , the peak of the optical lightcurve will occur when  $\Gamma \sim (\theta_{obs} - \theta_w)^{-1}$ . This model of the two component outflow could produce the rises observed in this sample.

In the case where the optical emission is produced in both the narrow and the wide components, the dominance of emission from one component over the other, depends

mostly on the energy within each component and on the viewing angle of the observer (for a more detailed description see Peng et al. (2005)). However, in this case as the emission is produced in both components, it is likely that on-axis and off-axis viewers will observe two peaks. This effect is not seen in the UVOT lightcurves in this paper and therefore, the jet is unlikely to have two components where both produce optical/UV emission.

## 5.2 The Late UVOT afterglow

A correlation has been observed between the observed magnitude at 400s and the decay after 500s. However, there is no significant evidence from a Spearman Rank test performed between  $\alpha_{>150s,rest}$  and the luminosity in the rest frame at 100s, for a similar correlation in the rest frame. For an off-axis jet, a correlation is expected between the luminosity and the decay of the lightcurve when the viewing angle is changed, with fainter, shallower afterglows having a larger viewing angle (Panaitescu & Vestrand 2008). As this data do not show a strong correlation of this type, this suggests that the outflows are viewed within the half-opening angle  $\theta$  or within a core of uniform energy density  $\theta_c$ . This supports the idea that the start of the forward shock produces the rises observed in the UVOT lightcurves. However, this does not give an indication of the geometry of the jet which may be uniform, comprise of two components, or be structured.

## 5.3 UVOT afterglow luminosity

The luminosity distribution found in this work shows no evidence for bimodality, which is in contradiction with the results of Nardini et al. (2006, 2008), Liang & Zhang (2006) and Kann et al. (2007), who all claim a bimodal distribution within their samples. However, the lack of evidence for bimodality within the distributions in this sample is consistent with the work of Cenko et al. (2008) and Melandri et al. (2008). Cenko et al. (2008) present a luminosity distribution at 1000s in the rest frame from a sample of 17 GRBs, with known redshift, observed with the Palomar 60 inch telescope. Their distribution shows no evidence for bimodality. Melandri et al. (2008) produce 3 luminosity distributions for 16 optical afterglows observed with the Liverpool and Faulkes telescopes. They find a single peaked luminosity distribution for three rest frame epochs: 10mins, 0.5 days and 1 day, which are well fit by a log-normal function. Melandri et al. (2008) do not correct their lightcurves for host extinction, but as discussed in this paper the correction for host extinction appears to have minimal effect on the luminosity distribution. Therefore, it is possible to compare the distributions of Melandri et al. (2008) with the distributions produced with this sample.

## 5.4 Comparison of the XRT and UVOT canonical lightcurves

There are three segments which are usually found in X-ray lightcurves within the first  $\sim 10^5$ s (Zhang et al. 2006; Nousek et al. 2006). The first segment is a fast, early decay with  $-5 < \alpha_{X1} < -3$ , typically ending within 100s-1000s after the trigger. The fast decay is thought to be caused by the tail of the prompt emission (Zhang et al. 2006; Nousek et al. 2006). The second segment is shallow with  $-1.0 < \alpha_{X2} < -0.5$  (although this range should now be considered as  $-1.0 < \alpha_{X2} < 0.0$ , Liang et al. 2007), ceasing between 1000s and 10000s and is attributed to energy injection (Zhang et al. 2006; Nousek et al. 2006). The third segment decays as  $-1.5 < \alpha_{X3} < -1$  and is expected to occur at the end of energy injection (Zhang et al. 2006; Nousek et al. 2006).

The range in temporal index of the optical lightcurve

before 500s, taken as the mean plus or minus the dispersion, is  $-1.17 < \alpha < 0.21$ . This range is clearly inconsistent with the first segment of the XRT canonical lightcurve. The range of temporal index before 500s is most similar to the range of the second segment of the XRT canonical model. However, none of the XRT canonical lightcurve segments indicate rising behaviour for the X-ray lightcurves. Applying the theoretical interpretations for the individual segments of the XRT canonical lightcurve, provided by Zhang et al. (2006) and Nousek et al. (2006), to the UVOT canonical lightcurve suggests that before 500s, the emission producing the optical lightcurves is from the forward shock and that a number of the UVOT afterglows during this period are energy injected. The lack of corresponding rising behaviour in the X-ray lightcurves, presuming an achromatic rise ( $\nu_m < \nu_{opt}$ ), suggests that the rise of the forward shock is masked in the X-rays, possibly by the contribution of the prompt emission. This is consistent with the model of Willingale et al. (2007) who suggest that the steep and shallow decays of the X-ray lightcurves are dominated by the prompt emission and afterglow emission respectively, and that they do not observe the rise of the afterglow emission as this is masked by the prompt emission.

In Section 4, the lightcurves after 500s were fitted with power-laws and broken power-laws. The GRBs which were best fitted by broken power-laws are discussed separately. For the optical lightcurves that decay as power-laws, the range in decay is  $-1.22 < \alpha < -0.52$ . Like the range in decay before 500s, the range in decay after 500s is most similar to the decay range of the second segment of the XRT canonical model. Assuming the same reasoning as for the XRT segments, this suggests that after 500s the optical lightcurves are consistent with emission from the forward shock and most of these are energy injected.

For the four GRBs that are best fit with a broken power-law after 500s, the range in temporal decay before the break is  $-0.74 < \alpha < -0.46$ , which is consistent with the range given for the second segment of the canonical XRT model. This suggests that before the break the optical lightcurves are energy injected. The range in the temporal decay after the break is  $-1.72 < \alpha < -1.34$ , which is consistent with the third decay of the XRT canonical lightcurve, which has been suggested to be the decay following the end of energy ejection.

## 6 CONCLUSIONS

In this paper we systematically reduced and analyzed a sample of 27 GRBs, which met a strict set of selection criteria. We note that the temporal behaviour of the optical afterglows in the sample is varied, with the greatest variation occurring in the early phase of the lightcurves: before 500s the lightcurves may rise or decay. The mean for  $\alpha_{<500s}$  is  $-0.48^{+0.15}_{-0.19}$  with a dispersion of  $0.69^{+0.19}_{-0.06}$ . However, after 500s, all the lightcurves decay. The lightcurves were fitted with power-laws and broken power-laws. A broken power-law was deemed to be an improvement, if the  $\chi^2/D.O.F$  decreased and the probability of chance improvement was small ( $< 1\%$ ) and in 5 cases a broken power-law was considered a better fit. The mean decay index after 500s, when including only those that decay with a single power-law, is

$-0.87_{-0.09}^{+0.10}$  with a dispersion of  $0.35_{-0.04}^{+0.10}$ . There is a correlation at 99.8% probability, between the magnitude at 400s and the temporal decay after 500s, with the brightest optical afterglows decaying the fastest.

We investigated the cause of the rising behaviour in the early afterglow and discussed the following physical mechanisms and geometric scenarios: the passage of the synchrotron frequency  $\nu_m$ , reverse shock, dust destruction, the start of the forward shock, the viewing angle of a (possibly structured) jet and a two component outflow. The rise in the optical lightcurves may be attributed to either the start of the forward shock, or to an off-axis viewing angle where the observer sees an increasing amount of emission as the Lorentz factor of the jet decreases. We also investigated the correlation between magnitude and decay after 500s. We determined that a correlation observed between the magnitude at 400s and the decay after 500s is only weakly dependent on redshift. A Spearman rank test performed between the luminosities at 100s and the decay after 150s in the rest frame did not reveal a significant correlation. However, a luminosity-decay correlation would be expected for jets viewed off-axis, where the more off-axis the jet the fainter and shallower the lightcurve. We do not observe a strong correlation of this type, suggesting that the optical lightcurves are produced by jets viewed on-axis and that the rise observed in the optical lightcurves is caused by the start of the forward shock.

We produced luminosity lightcurves for the 21 GRBs in the sample with known redshift. The luminosity lightcurves were produced at a common wavelength of 1600Å in the rest frame. We find that the logarithmic distribution of the luminosities at three rest frame epochs: 100s, 1000s and 10 ks do not show evidence for bimodality. Correcting the lightcurves for the host extinction increases the mean luminosities of the distributions, but does not considerably alter their appearance and the change in standard deviations of the logarithmic luminosity distributions is no greater than 0.08 for any of the three epochs. The lack of evidence for bimodality is consistent with the findings of Melandri et al. (2008) and Cenko et al. (2008).

Finally, we compared the temporal behaviour of the optical afterglows in this sample with the XRT canonical model. We have found that the temporal indices before 500s and the temporal indices of the lightcurves after 500s are most consistent with the the shallow decaying segment of the XRT canonical model. Nousek et al. (2006) and Zhang et al. (2006) suggest that the shallow decay segment of the XRT canonical model is energy injected. This would suggest that the optical lightcurves are energy injected as well. The lack of rises observed in X-ray afterglows could be due to the prompt emission masking them.

## 7 ACKNOWLEDGMENTS

This research has made use of data obtained from the High Energy Astrophysics Science Archive Research Center (HEASARC) and the Leicester Database and Archive Service (LEDAS), provided by NASA's Goddard Space Flight Center and the Department of Physics and Astronomy, Leicester University, UK, respectively. SRO acknowledges the support of an STFC Studentship. SZ thanks STFC for its support through an STFC Advanced Fellowship.

## REFERENCES

- Band D., Matteson J., Ford L., Schaefer B., Palmer D., Teegarden B., Cline T., Briggs M., 1993, *ApJ*, 413, 281  
 Barthelmy S. D., et al., 2005, *Space Science Reviews*, 120, 143  
 Berger E., Fox D. B., Cucchiara A., 2007, *GRB Coordinates Network*, 6470  
 Berger E., Kulkarni S. R., Rau A., Fox D. B., 2006, *GRB Coordinates Network*, 4815  
 Bloom J. S., Foley R. J., Kocevski D., Perley D., 2006, *GRB Coordinates Network*, 5217  
 Bloom J. S., Frail D. A., Sari R., 2001, *AJ*, 121, 2879  
 Bloom J. S., Perley D. A., Chen H. W., 2006, *GRB Coordinates Network*, 5826  
 Burrows D. N., et al., 2005, *Space Science Reviews*, 120, 165  
 Burrows D. N., et al., 2008, *ArXiv e-prints*, 0803.1844  
 Chen H.-W., Thompson I., Prochaska J. X., Bloom J., 2005, *GRB Coordinates Network*, 3709  
 Cenko S. B., Kelemen J., Harrison F. A., Fox D. B., Kulkarni S. R., Kasliwal M. M., Ofek E. O., Rau A., Gal-Yam A., Frail D. A., Moon D. ., 2008, *ArXiv e-prints*, 0808.3983  
 D'Alessio V., Piro L., Rossi E. M., 2006, *A&A*, 460, 653  
 de Pasquale M., et al., 2008, *MNRAS*  
 Fenimore E. E., Epstein R. I., Ho C., 1993, *A&A Suppl.*, 97, 59  
 Foley R. J., Chen H.-W., Bloom J., Prochaska J. X., 2005, *GRB Coordinates Network*, 3483  
 Fynbo J. P. U., Limousin M., Castro Cerón J. M., Jensen B. L., Naranen J., 2006, *GRB Coordinates Network*, 4692  
 Fynbo J. P. U., et al., 2005, *GRB Coordinates Network*, 3749  
 Giannios D., Mimica P., Aloy M. A., 2008, *A&A*, 478, 747  
 Golenetskii S., Aptekar R., Mazets E., Pal'Shin V., Frederiks D., Cline T., 2005a, *GRB Coordinates Network*, 3474  
 Golenetskii S., Aptekar R., Mazets E., Pal'Shin V., Frederiks D., Cline T., 2005b, *GRB Coordinates Network*, 4030  
 Golenetskii S., Aptekar R., Mazets E., Pal'Shin V., Frederiks D., Cline T., 2005c, *GRB Coordinates Network*, 4238  
 Golenetskii S., Aptekar R., Mazets E., Pal'Shin V., Frederiks D., Cline T., 2006a, *GRB Coordinates Network*, 5837  
 Golenetskii S., Aptekar R., Mazets E., Pal'Shin V., Frederiks D., Cline T., 2006b, *GRB Coordinates Network*, 5570  
 Golenetskii S., Aptekar R., Mazets E., Pal'Shin V., Frederiks D., Cline T., 2006c, *GRB Coordinates Network*, 5722  
 Golenetskii S., Aptekar R., Mazets E., Pal'Shin V., Frederiks D., Cline T., 2006d, *GRB Coordinates Network*, 5748  
 Golenetskii S., Aptekar R., Mazets E., Pal'Shin V., Frederiks D., Cline T., 2007, *GRB Coordinates Network*, 6344  
 Golenetskii S., Aptekar R., Mazets E., Pal'Shin V., Frederiks D., Ulanov M., Cline T., 2006, *GRB Coordinates Network*, 4989  
 Granot J., Panaitescu A., Kumar P., Woosley S. E., 2002, *ApJL*, 570, L61  
 Granot J., Ramirez-Ruiz E., Perna R., 2005, *ApJ*, 630, 1003  
 Huang Y. F., Wu X. F., Dai Z. G., Ma H. T., Lu T., 2004, *ApJ*, 605, 300  
 Jakobsson P., et al., 2006a, *A&A*, 460, L13

- Jakobsson P., Fynbo J. P. U., Tanvir N., Rol E., 2006, GRB Coordinates Network, 5716
- Jakobsson P., Levan A., Chapman R., Rol E., Tanvir N., Vreeswijk P., Watson D., 2006, GRB Coordinates Network, 5617
- Jaunsen A. O., Fynbo J. P. U., Andersen M. I., Vreeswijk P., 2007, GRB Coordinates Network, 6216
- Kalberla P. M. W., Burton W. B., Hartmann D., Arnal E. M., Bajaja E., Morras R., Pöppel W. G. L., 2005, *A&A*, 440, 775
- Kann D. A., et al., 2007, ArXiv e-prints, 0712.2186
- Klotz A., et al., 2008, *A&A*, 483, 847
- Kobayashi S., Mészáros P., Zhang B., 2004, *ApJL*, 601, L13
- Ledoux C., Vreeswijk P., Smette A., Jaunsen A., Kaufer A., 2006, GRB Coordinates Network, 5237
- Liang E., Zhang B., 2006, *ApJL*, 638, L67
- Liang E.-W., Zhang B.-B., Zhang B., 2007, *ApJ*, 670, 565
- Maccacaro T., Gioia I. M., Wolter A., Zamorani G., Stocke J. T., 1988, *ApJ*, 326, 680
- McMahon E., Kumar P., Piran T., 2006, *MNRAS*, 366, 575
- Melandri A., et al., 2008, *ApJ*, 686, 1209
- Mészáros P., 2006, *Reports of Progress in Physics*, 69, 2259
- Mészáros P., Rees M. J., 1997, *ApJ*, 476, 232
- Molinari E., et al., 2007, *A&A*, 469, L13
- Mundell C. G., et al., 2007, *ApJ*, 660, 489
- Nardini M., Ghisellini G., Ghirlanda G., 2008, *MNRAS*, 386, L87
- Nardini M., Ghisellini G., Ghirlanda G., Tavecchio F., Firmani C., Lazzati D., 2006, *A&A*, 451, 821
- Nousek J. A., et al., 2006, *ApJ*, 642, 389
- Oates S. R., et al., 2007, *MNRAS*, 380, 270
- Panaitescu A., 2005, *MNRAS*, 362, 921
- Panaitescu A., Kumar P., 2000, *ApJ*, 543, 66
- Panaitescu A., Kumar P., 2002, *ApJ*, 571, 779
- Panaitescu A., Vestrand W. T., 2008, *MNRAS*, 387, 497
- Pei Y. C., 1992, *ApJ*, 395, 130
- Peng F., Königl A., Granot J., 2005, *ApJ*, 626, 966
- Perna R., Lazzati D., 2002, *ApJ*, 580, 261
- Peterson B., Schmidt B., 2006, GRB Coordinates Network, 5223
- Poole T. S., et al., 2008, *MNRAS*, 383, 627
- Prochaska J. X., Chen H.-W., Bloom J. S., Falco E., Dupree A. K., 2006, GRB Coordinates Network, 5002
- Quimby R., Fox D., Hoefflich P., Roman B., Wheeler J. C., 2005, GRB Coordinates Network, 4221
- Ramirez-Ruiz E., Granot J., Kouveliotou C., Woosley S. E., Patel S. K., Mazzali P. A., 2005, *ApJL*, 625, L91
- Rees M. J., Mészáros P., 1992, *MNRAS*, 258, 41P
- Rees M. J., Mészáros P., 1994, *ApJL*, 430, L93
- Rol E., Jakobsson P., Tanvir N., Levan A., 2006, GRB Coordinates Network, 5555
- Roming P. W. A., et al., 2005, *Space Science Reviews*, 120, 95
- Roming P. W. A., et al., 2008, submitted *ApJ*
- Sakamoto T., et al., 2008, *ApJ Suppl.*, 175, 179
- Sakamoto T., et al., 2008, *ApJ*, 679, 570
- Sari R., 1997, *ApJL*, 489, L37+
- Sari R., Piran T., Narayan R., 1998, *ApJL*, 497, L17
- Sari R., Piran T., 1999, *ApJ*, 520, 641
- Sari R., Piran T., Halpern J. P., 1999, *ApJL*, 519, L17
- Schady P., et al., 2008, in preparation
- Schlegel D. J., Finkbeiner D. P., Davis M., 1998, *ApJ*, 500, 525
- Willingale R., et al., 2007, *ApJ*, 662, 1093
- Zhang B., Fan Y. Z., Dyks J., Kobayashi S., Mészáros P., Burrows D. N., Nousek J. A., Gehrels N., 2006, *Astrophys. J.*, 642, 354
- Zhang B., Kobayashi S., Mészáros P., 2003, *ApJ*, 595, 950
- Zhang B., Mészáros P., 2004, *International Journal of Modern Physics A*, 19, 2385